Regular evaporating black holes with stable cores

Alfio Bonanno

INAF, Osservatorio Astrofisico di Catania, via S.Sofia 78 and INFN,
Sezione di Catania, via S. Sofia 64, I-95123 Catania, Italy

Amir-Pouyan Khosravi and Frank Saueressig

Institute for Mathematics, Astrophysics and Particle Physics (IMAPP),
Radboud University, Heyendaalseweg 135, 6525 AJ Nijmegen, The Netherlands

A feature shared by many regular black hole spacetimes is the occurrence of a Cauchy horizon. It is then commonly believed that this renders the geometry unstable against perturbations through the mass-inflation effect. In this work, we perform the first dynamical study of this effect taking into account the mass-loss of the black hole due to Hawking radiation. It is shown that the time-dependence of the background leads to two novel types of late-time behavior whose properties are entirely determined by the Hawking flux. The first class of attractor-behavior is operative for regular black holes of the Hayward and renormalization group improved type and characterized by the square of the Weyl curvature growing as v^6 at asymptotically late times. This singularity is inaccessible to a radially free-falling observer though. The second class is realized by Reissner-Nordström black holes and regular black holes of the Bardeen type. In this case the curvature scalars remain finite as $v \rightarrow \infty$. Thus the Hawking flux has a profound effect on the mass-inflation instability, either weakening the effect significantly or even expelling it entirely.

I. INTRODUCTION

The resolution of spacetime singularities, omnipresent in solutions of general relativity [1], constitutes a key motivation for quantum gravity research. While first principle investigations of the mechanisms which could lead to singularity resolution are still scarce [2–6], there have been a number of phenomenologically motivated proposals for regular black hole geometries replacing the singular region by a patch of regular de Sitter space. Examples include the regular black hole geometries proposed by Dymnikova [7,8], Bardeen [9], renormalization group improved black hole spacetimes in the context of the gravitational asymptotic safety program [10] (also see [11–13] for recent developments and more references), Planck stars motivated from loop quantum gravity [14–16], the Hayward black hole [17], and extensions proposed by Koshelev *et al.* [18].[1] More recently, regular black hole spacetimes exhibiting a "Gauss" core have been proposed in [20].

Based on topological considerations, it is clear that any regular black hole solution exhibiting an asymptotically flat region and a de Sitter core must have an even number of horizons.[2] In the simplest case, this entails that there is an (outer) event horizon and an (inner) Cauchy horizon. This horizon structure is identical to the one of a charged Reissner-Nordström black hole.

This modification entails a drastic consequence for the final state of the black hole. When treated at the level of quantum field theory on a curved spacetime, black holes emit Hawking radiation, a perfect black body radiation whose temperature T is proportional to the surface gravity of the event horizon. As the Hawking radiation carries away energy, the black hole becomes lighter and T increases. Extrapolating the semiclassical analysis (assuming that the process is still adiabatic and neglecting the backreaction of the geometry) this process terminates with the complete evaporation of the black hole within a finite time if the geometry comes with a single horizon. The presence of a inner horizon changes this picture drastically; in this case the energy loss due to Hawking radiation leads to the two horizons approaching each other. For static, spherically symmetric geometries, the final state of the evaporation process is then a critical black hole remnant with a typical mass given by the Planck mass [10,17,22].[3] Reaching this final configuration requires an infinite timespan though. In this way, regular black holes may also

---

[1]Also see [19] for a review and further references.
[2]For recent work on the dynamical creation of horizons from the collapse to a regular black hole see [21].

[3]In the rotating case, the question about the final state is more complicated since the Hawking flux may first spin down the black hole and only subsequently carry away its mass [23].

024005-1

provide an elegant solution to the information loss problem in black hole physics based on remnant formation [24,25].

A central point of critique, challenging the phenomenological viability of such regular black hole solutions [26,27], originates from the mass-inflation effect, first investigated in the context of the Reissner-Nordström solution [28]. In short, the mass-inflation scenario considers a perturbation of the black hole geometry by outgoing null-radiation modeling, e.g., gravitational waves created in the black hole formation process and subsequently reflected by the potential barrier surrounding the black hole. These perturbations lead to an exponential growth of the mass function at the Cauchy horizon, ultimately generating a null singularity. While this scenario potentially resolves the ambiguities arising from extending geodesics beyond a Cauchy horizon [28,29], it also suggests that the geometries are not stable on the timescales associated with the black hole evaporation process. Extrapolating this scenario from the Reissner-Nordström geometry to regular black hole solutions then suggests that these could also suffer from the mass-inflation effect, leading to a dynamically generated spacetime singularity at the Cauchy horizon.

In [30], it was established that this conclusion is premature though. While the extrapolation works for certain classes of static regular black holes, including the geometries proposed by Bardeen, the Hayward geometry and renormalization group improved black hole solutions are free from mass inflation. In these cases the mass function at the Cauchy horizon grows polynomially in time only and the resulting curvature singularity may be integrable. Technically, this behavior can be traced back to the presence of a late-time attractor in the evolution equation for the mass-function at the Cauchy horizon, rendering this quantity finite at asymptotically late times.

The taming of the mass-inflation effect then suggests that the dynamics at the Cauchy horizon and the black hole evaporation process could happen on similar timescales. Thus, a more complete understanding of the actual dynamics mandates to take the Hawking evaporation process into account. Our work addresses this question for the first time. As our main result, we discover two classes of universal late-time behaviors whose properties are dictated by simple structural properties of the mass function and the universality of the Hawking effect. The late-time attractors governing the dynamics either lead to a polynomial growth of the squared curvature tensors or even renders these quantities finite. Interestingly, the latter behavior appears for the case of Reissner-Nordström geometry once the Hawking radiation is included. The final state of the black hole evaporation process is still a cold remnant.

The rest of our work is then organized as follows. The Ori model for mass-inflation [29] is reviewed in Sec. II. Sections III and IV contains a detailed discussion of the model in the context of an evaporating Hayward black hole and the Reissner-Nordström geometry, respectively. Other regular black hole geometries can be treated along similar lines and are discussed in Sec. V. Our conclusions and a brief outlook are given in Sec. VI. Technical details related to our analysis are given in three appendices with Appendix A summarizing the explicit expressions for the scalar curvature invariants, Appendix B giving the detailed results for the late-time attractors, and Appendix C analyzing the properties of radial geodesics in the black hole geometries.

II. THE ORI MODEL FOR MASS INFLATION

We start by reviewing the background material underlying the analysis in the main parts of our work. The line-element of a (generically nonstatic) spherically symmetric spacetime can be cast into a $2 + 2$ form,

$$ds^2 = g_{ab}(x^c)dx^a dx^b + r^2 d\Omega^2, \qquad (1)$$

where $d\Omega^2 = d\theta^2 + \sin^2\theta d\phi^2$ is the line element on the unit two-sphere, x^a, $a = 1, 2$, are coordinates in the submanifold $\theta = \phi = $ const, and $r(x^c)$ is the radius of the 2-sphere $x^a = $ const. A physically relevant quantity is the quasilocal Misner-Sharp mass function $M(x^c)$ defined via

$$g^{ab}\partial_a r \partial_b r = f(x^c) =: 1 - \frac{2M(x^c)}{r}. \qquad (2)$$

For a Schwarzschild black hole $M(x^c)$ agrees with the mass function m. Static, regular black hole geometries typically generalize this relation by promoting M to a function of the radial coordinate.

The mass-inflation phenomenon occurs when the inner horizon is perturbed by a cross-flow stream of lightlike matter. In a realistic gravitational collapse this combination of outgoing and ingoing flux is produced by the matter of the collapsing star and by the combined contribution of ingoing and outgoing gravitational waves [31]. In the optical geometric limit one can simply consider light-like pressureless matter and use a coordinate system adapted to the null-generators of the ingong radiation, so that $v = $ constant is an ingoing null ray. Ori has shown that the physics of the instability can be discussed assuming that the outgoing flux is modeled by an infinitesimally thin, pressureless null shell Σ. Albeit this assumption is valid in the optical geometric limit only, the model has the advantage to be analytically tractable in the $v \to \infty$ limit.

The shell Σ separates spacetime into two regions $\mathcal{M}_\pm$ with $(+)$ and $(-)$ referring to the regions inside and outside the shell, respectively. The metric in each sector can then be written as

$$ds^2 = -f_\pm(r, v_\pm)dv_\pm^2 + 2dr dv_\pm + r^2 d\Omega^2. \qquad (3)$$

The lapse function $f_\pm(r, v_\pm)$ in each sector depends on r and the ingoing Eddington-Finkelstein coordinate $v_\pm$ according

to (2). The equality of the induced metrics on Σ forces the radial coordinate r to be equal on both sides of the shell. The v-coordinates in the two regions are related by

$$f_+(r, v_+)dv_+ = f_-(r, v_-)dv_-, \qquad (4)$$

along Σ. This relation allows to express v_+ in terms of v_- and we chose to express the dynamics in terms of $v \equiv v_-$.

The position of the shell $R(v)$, as a function of v is governed by the first order differential equation

$$\dot{R}(v) = \frac{1}{2}f_-|_\Sigma, \qquad (5)$$

where the dot represents a derivative with respect to v. Furthermore, the Misner-Sharp mass in the two sectors separated by the shell are related by [29,32]

$$\frac{1}{f_+^2}\frac{\partial M_+}{\partial v_+}\bigg|_\Sigma = \frac{1}{f_-^2}\frac{\partial M_-}{\partial v_-}\bigg|_\Sigma \qquad (6)$$

with the v-derivatives evaluated before substituting the position of the shell. Using the identity (4), this relation can be expressed in terms of v,

$$\frac{1}{f_+}\frac{\partial M_+}{\partial v}\bigg|_\Sigma = F(v), \qquad (7)$$

with

$$F(v) = \frac{1}{f_-}\frac{\partial M_-}{\partial v}\bigg|_\Sigma. \qquad (8)$$

Equation (7) constitutes a first-order differential equation determining the dynamics of M_+ in terms of quantities given outside of the shell. Following Appendix A, M_+ determines the curvature in the inside region. Thus, there is a close relation between M_+ and observable quantities in the inner region of the shell. For later convenience, it is useful to write the left-hand side of Eq. (7), stressing its dependence on m_+,

$$\frac{1}{f_+}\frac{\partial M_+}{\partial v}\bigg|_\Sigma = \frac{1}{P(m_+)}\dot{m}_+. \qquad (9)$$

For the examples discussed in our work $P(m_+)$ is either linear or quadratic in m_+ with the coefficients of the polynomial depending on the model details.

Typically, the analysis of mass inflation considers a fixed background geometry of mass m_0, say, and adds a small perturbation to the mass function. The boundary condition at the event horizon is fixed through the Price tail behavior, so that [33,34]

$$m_-(v) = m_0 - \frac{\beta}{(v/v_0)^p} \qquad (10)$$

in the region outside the shell. Here $\beta > 0$ is a quantity with the dimension of a mass and v_0 sets the initial value of v. Furthermore, the exponent governing the decay of the perturbation depends on its angular momentum and one has $p \geq 11$.

The original studies of a fixed background geometry perturbed by an ingoing influx of energy appear to indicate that the Cauchy horizon is a generic surface of infinite blueshift [35]. Further investigations of gravitational wave perturbations near the Cauchy horizon confirmed the exponential divergence of the mass function and charged black holes with spherical symmetry, i.e., the Reissner-Nordström metric, have been shown to exhibit a curvature scalar singularity [28]. Furthermore Ori used an exact solution based on works of Poisson and Israel to show that the tidal forces at this singularity remain finite [29]. We stress that, strictly speaking, the Ori model building on the Price tail behavior (10) is valid for asymptotically late times v only. Therefore, conclusions drawn from the model in a regime where v is small and the perturbation significant compared to the mass m_0 have to be interpreted with care and should be confirmed by an analysis of the full dynamics [36].

Recently it is been shown in [30] that in fact the functional dependence of Misner-Sharp mass on m_+ determines the late-time behavior of these geometries. In particular, while a linear dependence leads to mass-inflation instability, a nonlinear relation leading to a quadratic polynomial $P(m_+)$ in Eq. (9) can tame the exponential growth of m_+ in the late-time regime.

III. MASS-INFLATION IN THE HAYWARD GEOMETRY

Upon introducing our dynamical framework, we now specialize to the case of the Hayward geometry [17]. The background geometry including the Hawking effect is introduced in Sec. III A and a sketch of the conformal diagram related to the model is shown in Fig. 1. The late-time dynamics of the model is discussed in Sec. III B and we corroborate our findings through a numerical analysis in Sec. III C. We then briefly comment on the strength of the curvature singularity in Sec. III D.

A. The dynamical background geometry

For the Hayward geometry, the lapse function is given by

$$f(r) = 1 - \frac{2M(r)}{r}, \qquad M(r) = \frac{mr^3}{r^3 + 2ml^2}. \quad (11)$$

Here M is the Misner-Sharp mass and m is the asymptotic mass of the configuration in Planck units where Newton's constant $G_N = 1$. Furthermore, l is a free parameter setting
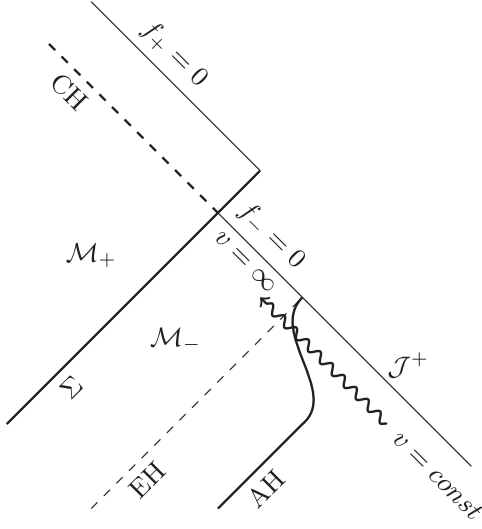
FIG. 1.   Schematic late advanced-times conformal geometry of our model. The event horizon (EH) and Cauchy horizon (CH) are indicated by the dashed lines while the position of the (time-dependent) apparent horizon (AH) has been added as the solid curve. Owed to the Hawking flux (indicated by the arrow) these quantities agree at asymptotically late times $v = \infty$. The shell Σ separates spacetime into an inner region $\mathcal{M}_+$ and an outer region $\mathcal{M}_-$. The spherically symmetric geometries in each sector are characterized by the lapse functions $f_\pm$, respectively.

the scale where the modifications of the geometry set in. The Schwarzschild geometry is recovered for $l = 0$ so that $M = m$ in this case.

The horizons of the geometry (11) appear as solutions of the horizon condition

$$2l^2 m - 2mr^2 + r^3 = 0. \tag{12}$$

For sufficiently large values m, there is an (outer) event horizon at r_+ and an (inner) Cauchy horizon at $r_- < r_+$. Their explicit position as function of the parameters m, l can be found by solving the cubic. The surface gravity at the horizons is defined as

$$\kappa_\pm = \pm \frac{1}{2} \frac{\partial f(r)}{\partial r}\bigg|_{r=r_\pm}, \tag{13}$$

where the signs are chosen such that $\kappa_\pm > 0$. For the critical mass (indicated by the subscript cr)

$$m_{cr} = \frac{3\sqrt{3}}{4} l, \tag{14}$$

the two horizons coincide and are located at

$$r_{cr} = \sqrt{3} l. \tag{15}$$

In this case, one obtains a cold remnant.

We now include the effect of the black hole evaporation through the emission of Hawking radiation. Following Hawking's seminal work [37], the event horizon emits Hawking radiation with temperature

$$T = \frac{1}{4\pi} \frac{\partial f}{\partial r}\bigg|_{r=r_+}. \tag{16}$$

We model this effect as ingoing radiation of negative energy which decreases the asymptotic mass of the black hole. The power radiated from the black hole follows from Boltzmann's law

$$P = \frac{\pi^2}{30} T^4 A, \tag{17}$$

where $A \equiv 4\pi r_+^2$ is the area of the event horizon. Promoting the temperature and horizon area to functions of v and using the adiabatic approximation the mass-loss of the geometry can be computed from

$$\frac{\partial m(v)}{\partial v} = -\frac{\pi^2}{30} T(v)^4 A(v), \tag{18}$$

where the area of the event horizon is approximated dynamically from the location of the apparent horizon in (12). Equation (18) turns into a closed equation determining the v-dependence of m. The late-time behavior can be determined analytically,

$$m(v) \simeq m_{cr} + \frac{10935 l^4 \pi}{8v} + \mathcal{O}(v^{-3/2}). \tag{19}$$

Here we have fixed the integration constant such that $m(v)$ approaches m_{cr} for asymptotically large values v. The full solution of (18) can be obtained by numerical integration and is shown in Fig. 2.

At this point, it is instructive to compare Eqs. (10) and (19). This reveals that perturbations following Price's law decay significantly faster than the power-law corrections to the critical mass. This suggests that it is actually the Hawking effect which dominates the asymptotic behavior.

B. Mass inflation: Identifying the late-time attractor

We are now in a position to evaluate the late-time dynamics of the Ori model for the background given by the (time-dependent) Hayward geometry. This can be conveniently done by analyzing the equations of motion using the Frobenius method. It then turns out that the resulting scaling behaviors are crucially modified by cancellations of leading and subleading terms obtained at earlier stages in the expansion. In order to obtain the full information one therefore has to compute the leading as well as several subleading terms controlling the late-time dynamics of the mass function $m_-(v)$ and $R(v)$. In order to
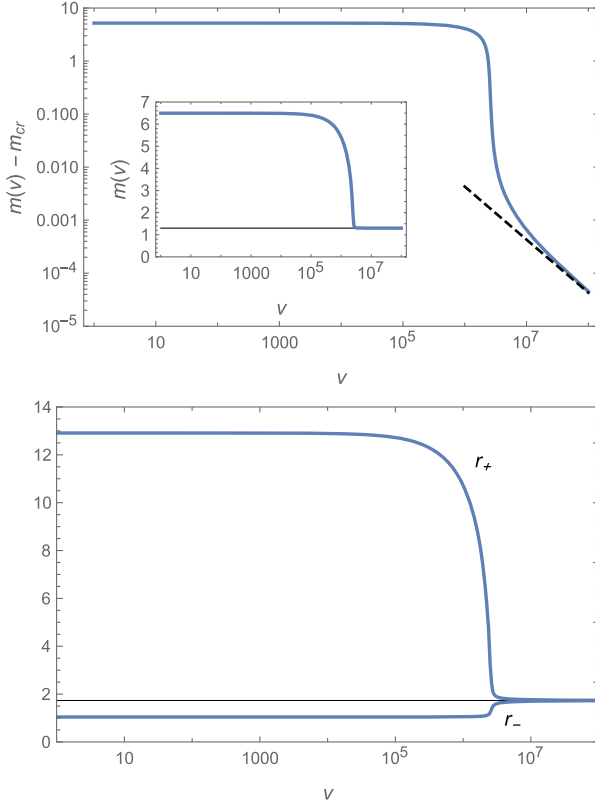
FIG. 2. Top diagram: illustration of $m(v) - m_{cr}$ resulting from numerically integrating Eq. (18) with initial condition $m(1) = 5m_{cr}$ and $l = 1$ (blue line). The black dashed line marks the asymptotic solution (19). For convenience, $m(v)$ approaching the critical mass m_{cr} (black horizontal line) is depicted in the inset. Bottom diagram: radial position of the apparent event horizon $r_+(v)$ (top curve) and apparent Cauchy horizon $r_-(v)$ (bottom curve). Asymptotically, the horizons approach the critical value r_{cr} depicted as the black horizontal line.

avoid giving bulky formulas, we are displaying the leading terms in the expansion only and indicate the fact that we are dealing with asymptotic expressions by the $\simeq$ symbol. The full expressions and additional technical comments underlying the analysis can be found in Appendix B.

We start with the mass-function in the region outside the shell, $m_-(v)$, adopting the late-time dynamics given in Eq. (19). Substituting a Frobenius ansatz shows that the asymptotic time dependence is given by

$$m_-(v) \simeq m_{cr} + \frac{480\pi m_{cr}^4}{v}. \tag{20}$$

The time-dependent mass function also contains the contribution associated with the shell. The Price law behavior is subleading to the time dependence induced by the Hawking effect though. Hence, this contribution is not visible in the asymptotic analysis.

In the next step, we specialize (5) to the Hayward geometry,

$$\dot{R}(v) = \frac{1}{2} - \frac{m_- R^2}{R^3 + 2l^2 m_-}, \tag{21}$$

and determine the asymptotics of the position of the shell. At this point, it is instructive to first look at the right-hand side for v fixed. The function f_- vanishes at the (v-dependent) apparent event and Cauchy horizons. Thus the shell cannot cross these values. For the final configurations both $r_\pm(v)$ approach r_{cr}. Thus, we expect that the asymptotic position of the shell is given by r_{cr}. The leading corrections describing the approach of the shell can be found by making a Frobenius ansatz,

$$R(v) = r_{cr} + \frac{1}{v^s} \sum_{n=0} r_n v^{-n}, \tag{22}$$

where s and r_n are numerical coefficients. Substituting this expansion into Eq. (5) and demanding the existence of a nontrivial solution fixes $s = 1/2$. This results in a quadratic equation for the numerical coefficient r_0 which has the solutions $r_0 = \pm 3\sqrt{15\pi} r_{cr}^{5/2}$. Thus the late-time asymptotics of $R(v)$ is

$$R(v) \simeq r_{cr} \pm 3r_{cr}\left(\frac{15\pi r_{cr}^3}{v}\right)^{1/2}. \tag{23}$$

The sign ambiguity indicates that the shell can approach r_{cr} either from above $r > r_{cr}$ or below $r < r_{cr}$. Both cases can be physically viable *a priori*.

Subsequently, we substitute Eqs. (20) and (23) into (7). This yields

$$\frac{\dot{m}_+}{(R^3 + 2l^2 m_+)(R^3 - 2m_+(R^2 - l^2))} = F(v) \tag{24}$$

with

$$F(v) \equiv \frac{\dot{m}_-}{(R^3 + 2l^2 m_-)(R^3 - 2m_-(R^2 - l^2))}. \tag{25}$$

This equation exhibits two values for m_+ where $\dot{m}_+$ vanishes. Keeping v fixed and finite, these values are given by the roots of the quadratic polynomial

$$P(m_+) = (R^3 + 2l^2 m_+)(R^3 - 2m_+(R^2 - l^2)). \tag{26}$$

Substituting the asymptotic expansions of $R(v)$ and $m_-(v)$ into Eq. (25) gives the following asymptotics for $F(v)$:

$$F(v) \simeq \pm 4m_{cr}\left(\frac{5\pi m_{cr}}{v}\right)^{1/2}. \tag{27}$$

Hence, the right-hand side of Eq. (24) vanishes as $v \to \infty$. As a consequence $m_+(v) \simeq \text{const}$ is an asymptotic solution.

In order to fix this constant, we then solve the differential equation

$$\frac{27l^2 \dot{m}_+}{27l^2 - 6\sqrt{3}lm_+ - 8m_+^2} = \pm 4m_{cr} \left(\frac{5\pi m_{cr}}{v}\right)^{1/2}, \quad (28)$$

which results from substituting the asymptotic expansions (20), (23), and (27) into (7) and retaining the terms leading in $1/v$ only. Taking into account the sign ambiguity in (23), the resulting asymptotic solutions for m_+ are

$$m_+^{\text{asym}} = -\frac{m_{cr}}{2} (1 \mp 3 \tanh(6\sqrt{5\pi m_{cr} v} + c)), \quad (29)$$

where c is an integration constant. This constant drops out in the limit where $v \to \infty$. Thus, for a shell approaching r_{cr} from above

$$\lim_{v \to \infty} m_+(v) = m_{cr}, \quad (30)$$

while a shell approaching r_{cr} from below leads to the attractor

$$\lim_{v \to \infty} m_+(v) = -2m_{cr}. \quad (31)$$

These correspond to the two roots of (26) when evaluated at asymptotically late times. In particular, Eq. (31) generalizes the attractor taming mass inflation in the nondynamical setting [30], to the case of an evaporating black hole. The subleading correction to (31) is found by the Frobenius analysis described in Appendix B and reads

$$m_+(v) \simeq -2m_{cr} + 48 \sqrt{\frac{5\pi m_{cr}^5}{v}}. \quad (32)$$

We proceed with analyzing the asymptotics of the physical quantities including the curvature scalars computed in Appendix A. We distinguish the cases where the shell approaches r_{cr} from above (upper signs) and below (lower signs). We start by discussing the upper sign. In this case the Misner-Sharp mass remains finite

$$M_+(r, v)|_\Sigma \simeq \frac{2m_{cr}}{3}. \quad (33)$$

Consequently, the curvature invariants remain finite as well and evaluate to

$$C^2|_\Sigma \simeq \frac{2160\pi}{m_{cr} v}, \qquad K|_\Sigma \simeq \frac{81}{32m_{cr}^4}. \quad (34)$$

The v-independent terms in this expansion agree with the curvature scalars evaluated at the critical radius of the critical configuration. Hence, any perturbation which falls onto r_{cr} from above does not have any destabilizing effects on the geometry.

For the lower sign, the asymptotic behavior drastically differs. Substituting the asymptotic expansions into the general expression of the Misner-Sharp mass and evaluating at the position of Σ, we have

$$M_+(r, v)|_\Sigma \simeq -v. \quad (35)$$

While $M_+(r, v)$ is generically finite, it diverges in the limit $v \to \infty$ when evaluated at $r = r_{cr}$ due to a cancellation of the leading terms in the denominator. This divergence is much milder than the one encountered in the standard mass-inflation effect where M_+ grows exponentially in v.

The divergence (35) also propagates into the scalar curvature invariants. In particular

$$C^2|_\Sigma = \frac{19683v^6}{4096m_{cr}^{10}}, \qquad K|_\Sigma = \frac{59049v^6}{4096m_{cr}^{10}}. \quad (36)$$

Thus, again, the divergence is power law and not exponential. Remarkably, the results (35) and (36) are universal in the sense that they are independent of any free parameter. Hence any solution entering into this late-time scaling regime must follow this attractor behavior.

C. Mass inflation: Full numerical treatment

Following up on the asymptotic analysis of the previous section, we proceed with a numerical investigation of the dynamics. We start by constructing $m_-(v)$ in the outer sector of the shell by superimposing the mass loss due to Hawking radiation and the perturbation due to the shell

$$m_-(v) = m_{\text{Hawking}}(v) - \frac{\beta}{v^p}. \quad (37)$$

Here $m_{\text{Hawking}}(v)$ is obtained from solving Eq. (18) numerically with the boundary condition $\lim_{v \to \infty} m_{\text{Hawking}}(v) = m_{cr}$ according to Eq. (19). For concreteness, we take $\beta = 1$, $l = 1$, and $p = 11$. The resulting function $m_-(v)$ is then depicted in Fig. 3. This shows that the Price tail perturbation is only operative at values v much smaller than the time-scale set by the Hawking effect. This is in agreement with the result of the previous subsection that the late-time behavior of $m_-(v)$ is controlled by the Hawking effect only.

Given $m_-(v)$, we solve Eq. (5) to trace the position of the shell in the background geometry. We consider a shell situated between the apparent event horizon and Cauchy horizon. Choosing the initial mass of the unperturbed configuration as $m_{\text{Hawking}}(1) = 5m_{cr}$ and imposing initial conditions at $v_{\text{init}} = \{1, 10^4, 10^6\}$, typical trajectories $R(v)$ are displayed in Fig. 4. The solutions exhibit several phases which are universal in the sense that they are independent of the initial conditions. At early times, the shell falls towards smaller values of r, approaching the apparent
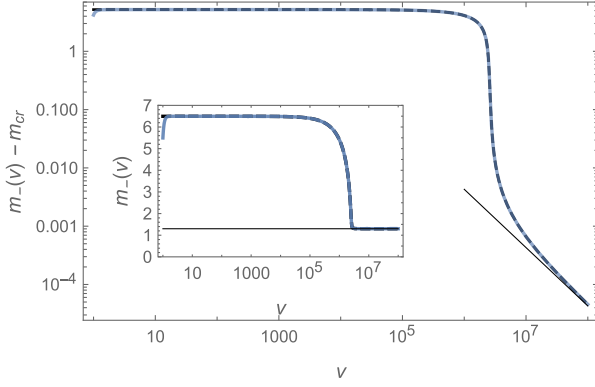
FIG. 3. Illustration of the background geometry $m_-(v) - m_{cr}$ resulting from (37) for $\beta = 1$ (blue curve) and $\beta = 0$ (dashed) for $l = 1$ in a log-log-plot. The solid line gives the asymptotic behavior (19). Inset: $m_-(v)$ for $\beta = 1$ (blue curve) and $\beta = 0$ (dashed) with the solid line showing m_{cr}. The perturbation due to the Price tail corrections vanishes at very short timescales so that the lines agree for $v \gtrsim 10$.

Cauchy horizon of the time-dependent geometry. Subsequently, the solutions trail $r_-(v)$ until they settle on the late-time attractor (23). Note that for late times we have $\dot{R}(v) > 0$ indicating that the late-time dynamics is actually governed by the minus sign in Eq. (23).

Specifying (7) to the Hayward geometry then leads to the following equation determining the mass function $m_+(v)$ inside the shell

$$\dot{m}_+ = \frac{(2l^2 m_+ + R^3)(R^3 - 2(R^2 - l^2)m_+)}{(2l^2 m_- + R^3)(R^3 - 2(R^2 - l^2)m_-)} \dot{m}_-. \quad (38)$$

Substituting the solutions for $m_-(v)$ and the dynamics $R(v)$, allows to solve this equation numerically. For the

latter, we adopt select the shell moving along the top (blue) curve in Fig. 4. Depending on the initial value for m_+^{init}, the numerical integration identifies two classes of solutions. Solutions starting with $m_+^{\text{init}} < m_+^{\text{crit}}$ terminate at finite v. Solutions where $m_+^{\text{init}} \geq m_+^{\text{crit}}$ exist for all values v and follow the attractor (31) at late times. A series of solutions taken from the class $m_+^{\text{init}} \geq m_+^{\text{crit}}$ are illustrated in Fig. 5. Notably, the information on the initial conditions is wiped out rather quickly as the shell settles on $r_-(v)$. As a result the dynamics becomes essentially universal for $v \geq 100$. For late times the solutions settle on the attractor (32).

Given the explicit expression for $m_+(v)$, it is now straightforward to determine the resulting Misner-Sharp mass $M_+(v)|_\Sigma$ and the explicit form of the curvature scalars (A4) and (A5). This data is shown in Figs. 6 and 7, respectively. The Misner-Sharp mass undergoes a transition from small to rather large values as the shell impacts onto $r_-(v)$. This can be traced back to the denominator in (11) becoming small (but not zero though). This behavior is transmitted into the curvature scalars which undergo a rapid increase during this transition before remaining at large constant values. This feature reflects the exponential grows of the Misner-Sharp mass reported in [38,39]. It precedes the attractor behavior for the curvature reported in the previous section.

At this point we stress that strictly speaking initial conditions for the dynamics should only be imposed at late time where the Ori model is capable of providing an accurate description of dynamics. The global analysis in this section clearly reveals that extrapolating the Ori model to early times may lead to misleading conclusions about the late-time behavior. This is particularly striking for solutions which hit a singularity before actually reaching the late-time attractor of the model.
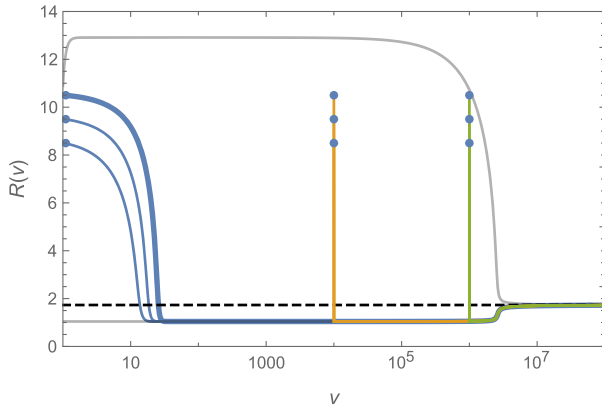

FIG. 4. Typical trajectories $R(v)$ describing the motion of shells with initial conditions marked by the blue dots at $v = 1$ (blue series), $v = 10^4$ (orange) and $v = 10^6$ (green) in a background where $m_{\text{Hawking}}(1) = 5m_{cr}$. The apparent event and Cauchy horizons are depicted as opaque gray lines while r_{cr} is given by the dashed line. All shells settle at r_{cr} at asymptotically late times.
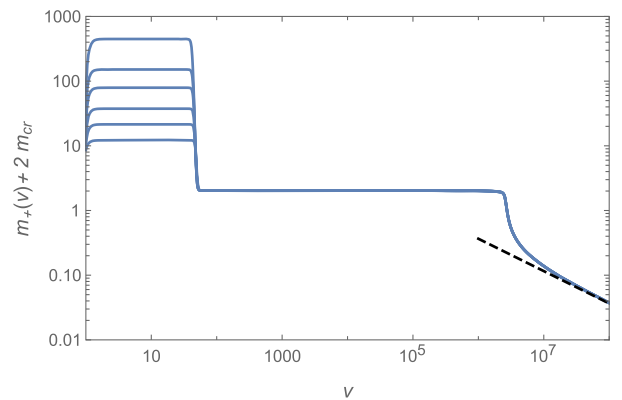

FIG. 5. Time evolution of $m_+(v)$ arising from solving (38) in the background provided by (37) and the shell moving along the thick blue curve depicted in Fig. 4. Initial conditions are imposed at $v = 1$ and chosen such that $m_+(1)$ is larger than the critical value required for the solutions reaching the late-time attractor (31). The dashed line indicates the asymptotic scaling behavior (32).
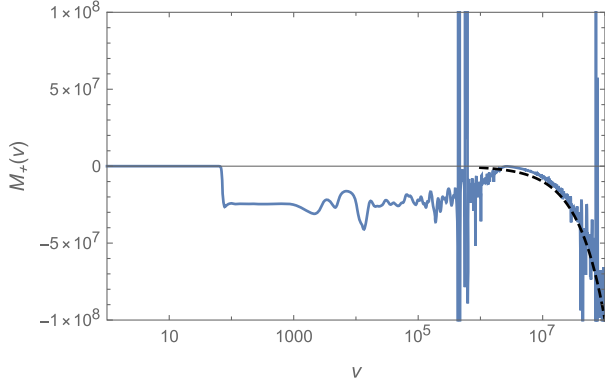
FIG. 6. Time-evolution of the Misner-Sharp mass evaluated in the inner sector of the shell. The rapid increase in the curvature is triggered by the shell aligning with the dynamical Cauchy horizon. The attractor behavior taming $M_+(v)|_\Sigma$ sets in when the background reaches the final stage of black hole evaporation and is preceded by a rapid decrease of $M_+(v)|_\Sigma$. The late-time attractor (35) is added as the dashed line. The wiggles exhibited by $M_+(v)$ should be interpreted as numerical artifacts. Their occurrence can be traced by to the denominator structure of $M_+(v)$ where the dynamics is essentially governed by the cancellation of two numerical quantities of order unity to very high precision. Hence, $M_+(v)$ is particularly sensitive to small errors in the numerical solutions of the differential equations. While this shows up in local wiggles, this does not affect the overall dynamics though.

D. Strength of the curvature singularity

It is interesting to discuss the implications of our findings with regard to possible extensions of the geometry beyond the Cauchy horizon. In the standard Poisson-Israel model [28], as first realized by [29] and further discussed by [40], the Cauchy singularity does not meet the necessary conditions to be strong in the Tipler sense [41]. In particular the tidal distortion experienced by an observer crossing the singularity is finite. In fact it is not difficult to find a coordinate transformation that renders the metric regular in the future sector of the shell [36]. However, the singularity is still strong in the Królak sense because the expansion of the null congruence is (negatively) diverging at the Cauchy horizon [40].

In the case of regular black holes the exponential divergence of the classical Poisson-Israel model is modified into a power-law divergence of the type $\sim v^{6p}$, with $v \to \infty$ where $p \geq 11$, and the singularity is Królak-weak [30]. Equation (36) confirms this picture once the effect of the Hawking flow, corresponding to $p = 1$ in the notation (10), is taken into account. This supports the idea that the strength of the inner horizon singularity in regular black holes is much milder than in the standard case. Moreover, it is completely fixed by the properties of the Hawking radiation at late advanced times. On the other hand, because our geometry is very close to the extremality, it is not difficult to show that, at variance with the
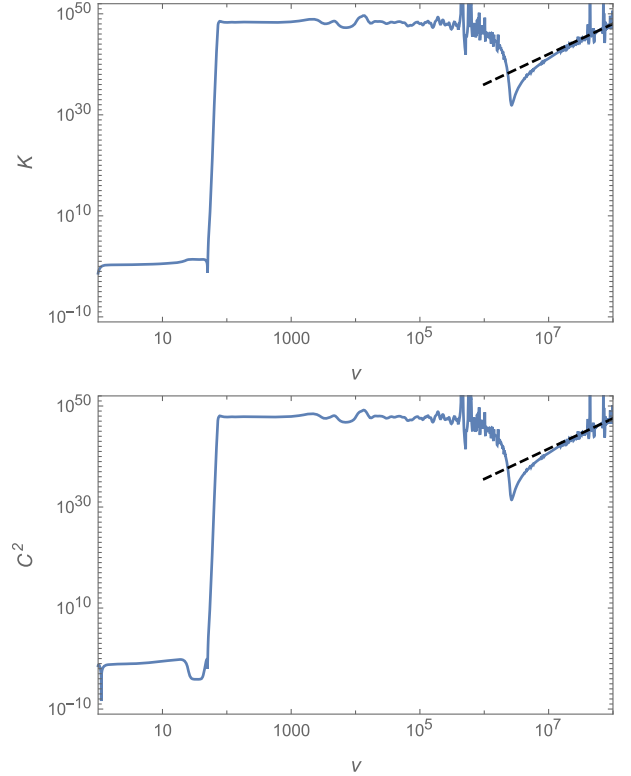

FIG. 7. Time evolution of the curvature scalars (A4) and (A5) evaluated in the inner sector of the shell. The rapid increase in the curvature is triggered by the shell aligning with the dynamical Cauchy horizon. The power-law scaling (36) has been added as a dashed line. Again the wiggles on the curve should be understood as numerical artifacts resulting from precise cancellations of quantities computed numerically.

nonextremal case, this singularity is never reached in a finite amount of proper time because $\tau \propto v$ as discussed in Appendix C.

In this context, it is interesting to note that the weakening of the singularity induced by the mass-inflation effect has also been observed for Reissner-Nordström black holes in the presence of a positive cosmological constant, see [42] and references therein. At the classical level, the cosmological constant induces an exponential damping of the perturbations close to the Cauchy horizon which then competes with the instability, lowering the degree of divergence in (some components of) the stress-energy tensor. As a consequence, it was argued that spacetime may admit an extension beyond the Cauchy horizon. This picture is challenged once the problem is elevated to the level of quantum field theory in curved spacetime. It was found in [43] that the quantum stress-energy tensor actually restores the mass-inflation singularity. This indicates that quantum effects may play a crucial role in determining whether spacetime can be continued across the Cauchy horizon. The corresponding investigation is beyond the scope of this article and will be left for future work.

IV. MASS INFLATION FOR THE REISSNER-NORDSTRÖM GEOMETRY REVISITED

An important insight obtained from the previous section is that the late-time behavior of $m_-(v)$ and $R(v)$ is controlled by the Hawking effect. In particular, the dynamics induced by the time-dependent background changes the late-time behavior from $\dot{R}(v) < 0$ to $\dot{R}(v) > 0$. This qualitative change warrants revisiting the mass-inflation effect in the (classical) Reissner-Nordström geometry, where it has been established initially using a static background [28,29]. The analysis follows the steps of the previous section. As the main result, we demonstrate that the mass inflation is absent once the dynamics of the background is introduced.

A. Geometry and late-time attractors

The line-element of the Reissner-Nordström geometry is again of the form (1) with the lapse function

$$f(r) = 1 - \frac{2m}{r} + \frac{Q^2}{r^2}, \qquad M = m - \frac{Q^2}{2r}. \qquad (39)$$

Here Q is the electric charge of the configuration. Similarly to the Hayward geometry, the Reissner-Nordström geometry possesses an event horizon and a Cauchy horizon situated at

$$r_\pm = m \pm \sqrt{m^2 - Q^2}. \qquad (40)$$

For $m^2 = Q^2$ the two horizons coincide and one obtains an extremal black hole with

$$m_{cr} = Q, \qquad r_{cr} = Q. \qquad (41)$$

For $m^2 > Q^2$ the event horizon again emits Hawking radiation with temperature given by (16). This leads to a mass loss described by (18).

The dynamics of the shell and geometry in its interior sector is again captured by Eqs. (5) and (7). Adapting these to the geometry (39), one arrives at the following system of coupled differential equations

$$\dot{R} = \frac{R^2 + Q^2 - 2Rm_-}{2R^2},$$
$$\dot{m}_+ = \frac{R^2 + Q^2 - 2Rm_+}{R^2} F(v), \qquad (42)$$

where

$$F(v) = \frac{R^2 \dot{m}_-}{R^2 + Q^2 - 2Rm_-}. \qquad (43)$$

Note that we have suppressed the v-dependence of m_- arising from the Hawking effect and the Price tail perturbation.

Determining the asymptotics of the resulting solutions based on the Frobenius method is then rather straightforward. The mass function approaches m_{cr} with the leading corrections falling off proportional to $1/v$,

$$m_-(v) \simeq m_{cr} + \frac{30\pi m_{cr}^4}{v} + O(v^{-3/2}). \qquad (44)$$

The shell approaches r_{cr} according to

$$R(v) \simeq r_{cr} - \frac{2\sqrt{15\pi} r_{cr}^{5/2}}{\sqrt{v}} + O(v^{-1}). \qquad (45)$$

The last relation already anticipates that the shell crosses r_{cr} and subsequently approaches the critical radius from $R(v) < r_{cr}$. Based on these relations, one obtains that

$$F(v) \simeq -\sqrt{\frac{15\pi m_{cr}^3}{v}} + O(v^{-1}), \qquad (46)$$

i.e., $F(v)$ vanishes asymptotically. This has profound consequences for the mass function in the inner sector of the shell. Consistency of (42) requires that

$$m_+(v) \simeq m_{cr} + \frac{30\pi m_{cr}^4}{v}, \qquad (47)$$

which goes hand-in-hand with $(Q^2 + R^2 - 2Rm_+) \simeq \mathcal{O}(v^{-3/2})$.

The crucial difference to the Hayward model then comes with the explicit form of the scalar curvature invariants tabulated in Table II. For the Reissner-Nordström case the denominators appearing in $K|_\Sigma$ and $C^2|_\Sigma$ remain finite. As a result the asymptotic limit of both curvature scalars remains finite as $v \to \infty$,

$$K|_\Sigma \simeq \frac{8}{m_{cr}^4} + \mathcal{O}(v^{-1/2}),$$
$$C^2|_\Sigma \simeq \frac{2880\pi}{m_{cr} v} + \mathcal{O}(v^{-3/2}). \qquad (48)$$

This is in striking difference with the standard mass-inflation effect where the curvature grows exponentially in v.

We now solve the system of equations (42) numerically, using a superposition of the Hawking radiation and Price tail perturbation for $m_-(v)$. We first consider a shell with initial conditions imposed at $v = 1$, even though this is out of the validity-range of the Ori model. The motion of this shell is quantitatively identical to the Hayward case shown in Fig. 4. The shell starts from its initial point, quickly falls towards the apparent Cauchy horizon, and eventually traces $r_-(v)$ into the asymptotic scaling regime.

The function $m_+(v)$ obtained from the early-time initial conditions is then displayed in Fig. 8. This shows that
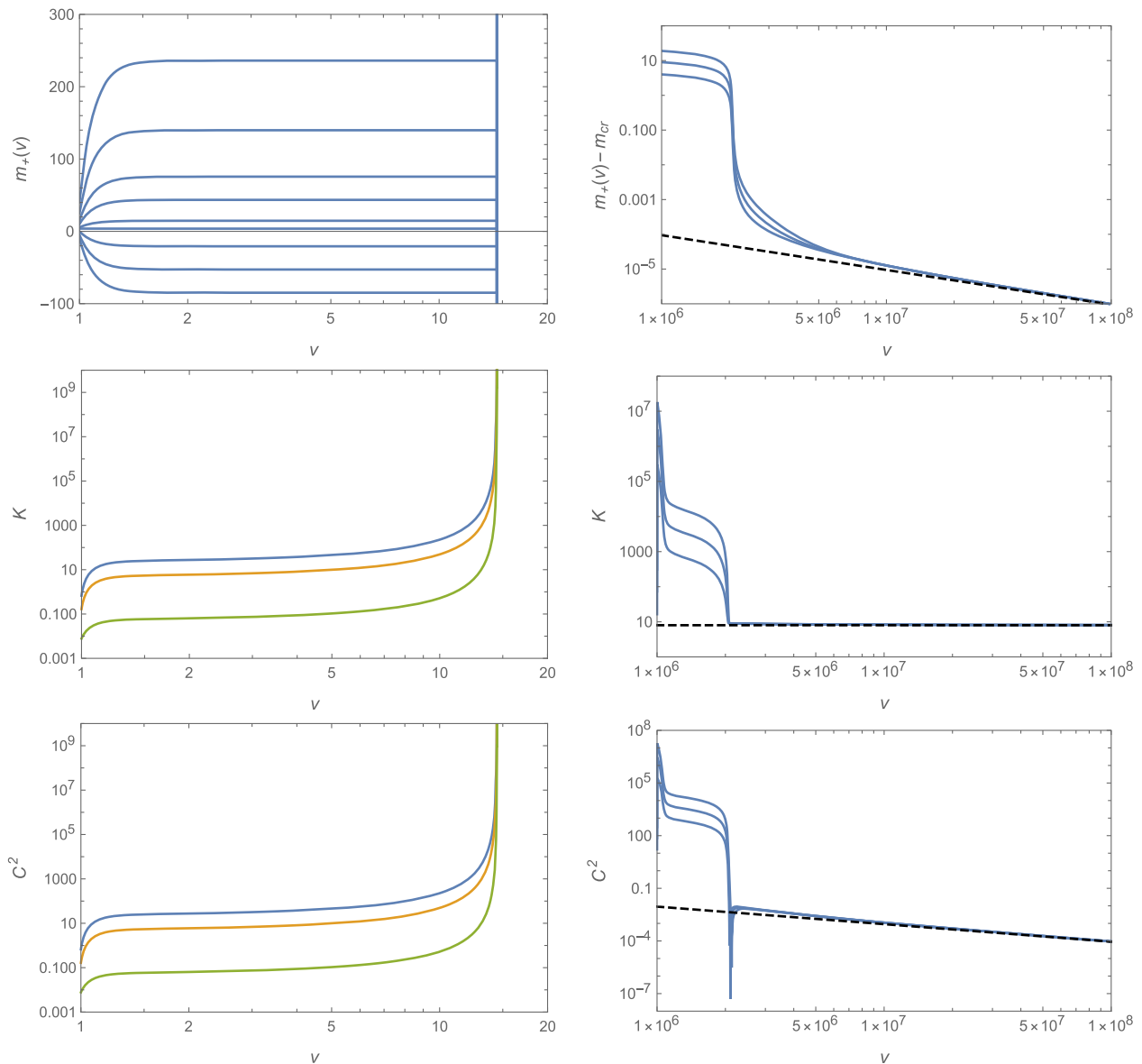
FIG. 8. Illustration of the mass-inflation effect for the Reissner-Nordström black hole including the Hawking flux in the background geometry. Initial conditions are imposed at early times $v = 1$ (left column) and late times $v = 10^6$ (right column). The top, middle, and bottom row show the time evolution of $m_+(v)$, $K|_\Sigma$ and $C^2|_\Sigma$, respectively. The early time dynamics depicts the evolution of $m_+(v)$ evaluated for the shell moving along $R(v)$ generated from the initial condition $R(1) = 7.5$ for varying initial conditions for m_+. Notably, $m_+(v)$ first moves along a plateau before exhibiting a rapid increase when the shell impacts on the apparent Cauchy horizon. This process induces a singularity in $m_+(v)$ situated at approximately $v \approx 14.5$. The divergence of m_+ induces a divergence in the curvature scalars when the shell impacts on the apparent Cauchy horizon. The dynamics following from initial conditions imposed at late times differs drastically: in this case $m_+(v)$ reaches the attractor regime (47), indicated by the dashed line. As a result $K|_\Sigma$ remains constant and $C^2|_\Sigma$ vanishes at asymptotically late times, cf. (48).

$m_+(v)$ first approaches a constant plateau whose value depends on the initial conditions imposed for m_+. Subsequently, the solution terminates in a singularity when the shell impacts on the apparent Cauchy horizon. As illustrated in the left column of Fig. 8, the divergence of m_+ induces a divergence in the curvature scalars. Thus, imposing initial conditions at early times leads to solutions

which terminate before reaching the late-time attractor identified in the Frobenius analysis.

On the right column of Fig. 8, this picture changes radically since the initial conditions are imposed at late-times within the validity range of the Ori model. In order to illustrate this, we solve the same dynamical system with initial conditions imposed at $v = 10^6$. At this point the

black hole background and in particular $m_-(v)$ and $R(v)$ are already very close to the attractor regime. As shown in the top-right diagram of Fig. 8, this induces the late-time attractor behavior for $m_+(v)$. As a consequence the curvature scalars shown in the middle-right and bottom-right diagram of the figure remain finite. Thus the Reissner-Nordström black hole does not develop a dynamical singularity once the effect of Hawking radiation is taken into account.

V. OTHER REGULAR BLACK HOLE GEOMETRIES

We complete our analysis by discussing two additional proposals for regular black holes, the renormalization group (RG)-improved black hole solutions [10] and the Bardeen black hole [9,44]. In these cases the lapse functions take the explicit form

$$f = 1 - \frac{2mr^2}{r^3 + \omega(2r + 9m)}, \quad M = \frac{r^3}{r^3 + \omega(2r + 9m)}, \quad (49)$$

and

$$f = 1 - \frac{2mr^2}{(r^2 + a^2)^{3/2}}, \quad M = \frac{r^3}{(r^2 + a^2)^{3/2}}, \quad (50)$$

respectively. In order to simplify the analysis we set $\omega = 1$ and $a = 1$. While this leads to significant simplifications when analyzing the structure of the equations, fixing the overall scale of the problem still allows to extract the generic features of the dynamics.

The analysis of the Ori model for these spacetimes proceeds completely analogous to the previous sections. In particular, the late-time expansion of the mass-function $m_-(v)$ and the motion of the shell are universal in the sense that the leading and subleading terms do not contain free integration constants. The motion of the shell again follows the behavior shown in Fig. 4. The decisive element in the

analysis is then given by the structure of the dynamical equation (7) determining the mass-function in the inner sector of the shell. For the RG-improved black hole the resulting first-order equation for $m_+(v)$ is

$$\dot{m}_+ = \frac{(9m_+ + R^3 + 2R)((9 - 2R^2)m_+ + R^3 + 2R)}{(9m_- + R^3 + 2R)((9 - 2R^2)m_- + R^3 + 2R)}\dot{m}_- \quad (51)$$

while for the Bardeen black hole one has

$$\dot{m}_+ = \frac{(R^2 + 1)^{3/2} - 2R^2 m_+}{(R^2 + 1)^{3/2} - 2R^2 m_-}\dot{m}_-. \quad (52)$$

Two observations are in order. Firstly, (51) gives rise to a polynomial $P(m_+)$ which is quadratic in m_+. Moreover, a comparison to the curvature invariants given in Table II shows that the factor $9m_+ + R^3 + 2R$ is the one appearing in the denominators of K and C^2. A consistent solution for m_+ then requires that this factor vanishes proportionally to v^{-1}. This causes a power-law divergence in $K|_\Sigma$ and $C^2|_\Sigma$ which is qualitatively identical to the one found for the Hayward black hole. Thus the late-time behavior of the two geometries follows the same universality class.

In the case of the Bardeen black hole a consistent solution of (52) again requires that $(R^2 + 1)^{3/2} - 2R^2 m_+ \propto v^{-1}$. The crucial difference in this case is that this factor does not constitute the denominator in the curvature scalars. As a result $K|_\Sigma$ and $C^2|_\Sigma$ remain finite in the inner sector of the shell. This is identical to the late-time behavior found the Reissner-Nordström black hole. Thus, these two geometries also give rise to the same universal late-time behavior close to the Cauchy horizon. The two geometries come with one crucial difference though; the Reissner-Nordström geometry hosts a spacetime singularity at its center while the Bardeen geometry satisfies the limiting curvature hypothesis everywhere. Thus the Bardeen black hole constitutes a prototypical example of a regular black hole where the mass-inflation effect does not induces a curvature singularity

TABLE I. Properties of the late-time attractor controlling the scaling of the curvature in the inner sector of the shell. The evaluation of the RG-improved black holes and the Bardeen black hole is given for the model parameters $\omega = 1$ and $a = 1$. The column $K|_\Sigma^\infty$ gives the scaling of the Kretschmann scalar evaluated in the limit $v \to \infty$. Note that the late-time behavior organizes itself in terms of two distinguished universality classes. For the Hayward and RG-improved geometry $K|_\Sigma \propto v^6$ while for the Reissner-Nordström and Bardeen geometry the curvature scalar remains finite.

	$f(r)$	$F(v)$	$K|_\Sigma^\infty$	$P(m_+)$	Early solutions reach late-time attractor
Reissner-Nordström	$1 - \frac{2m}{r} + \frac{e^2}{r^2}$	$\simeq -\sqrt{\frac{15\pi m_{cr}^3}{v}}$	$\propto v^0$	Linear	No
Hayward solution [17]	$1 - \frac{2mr^2}{r^3 + 2ml^2}$	$\simeq -\sqrt{\frac{80\pi m_{cr}^3}{v}}$	$\propto v^6$	Quadratic	Yes
RG improved black holes [10]	$1 - \frac{2mr^2}{r^3 + \omega(2r + 9m)}$	$\simeq -84.5 v^{-1/2}$	$\propto v^6$	Quadratic	Yes
Bardeen black hole [9,44]	$1 - \frac{2mr^2}{(r^2 + a^2)^{3/2}}$	$\simeq -19.2 v^{-1/2}$	$\propto v^0$	Linear	No

at asymptotically late times. For convenience, we have summarized the key features of the two universality classes and their representatives in Table I.

VI. SUMMARY AND OUTLOOK

In this work we studied the Ori model for mass inflation for regular black holes. As a novel feature, our analysis includes the mass-loss of the background geometry due to the emission of Hawking radiation. As a result, the asymptotic state of the geometries is an extremal black hole where the event and Cauchy horizons coincide at asymptotically late times. These configurations come with a finite mass, vanishing surface gravity, and zero Hawking temperature, i.e., they correspond to a cold remnant.

We demonstrated that the fact that the asymptotic geometry is an extremal black hole has profound consequences for the late-time dynamics of the mass-inflation effect. The function $F(v)$ controlling the dynamics of the mass function in the inner sector of the shell vanishes asymptotically, see Table I. This is at variance with the analysis of the same model on a static, noncritical background [30] where $F(v)$ asymptotes to a constant proportional to the surface gravity at the Cauchy horizon. As a consequence of this modification, we discover two classes of universal late-time behavior. In the first class curvature scalars including the Kretschmann invariant exhibit a power-law instead of an exponential growth. This class is realized by the Hayward and RG-improved black holes. In the second class the curvature scalars remain finite at asymptotically late times. This occurs for the Reissner-Nordström solution and Bardeen-type black holes. The fact that the final configuration is an extremal black hole furthermore suggests that radial geodesics do not encounter these singularities in a finite proper time.

A crucial question raised in [38,39], is whether the dynamical system can actually reach this salient late-time attractor. Our numerical analysis indicates that the dynamics of the shell and the Hawking effect operate on different timescales. The impact of the shell onto the apparent Cauchy horizon occurs on much shorter timescales as the evaporation of the black hole. This feature is universal and does not depend on details of the black hole geometry, cf. Fig. 4. Imposing the perturbation at late times, where we expect that the Ori model gives a valid description, we demonstrated that the salient late-time attractor quenching the mass-inflation singularity is reached in all geometries investigated in this work. These include the Hayward black hole, RG improved black hole, the Reissner-Nordström geometry, and Bardeen-type black holes.

For future investigations, it would be interesting to understand whether there is a mechanism taming the growth of the mass function triggered by the shell impacting on the Cauchy horizon. Refs. [45,46] proposed to achieve this by converting the Cauchy horizon to a degenerate horizon with vanishing surface gravity akin to

the horizon structure appearing in the final states of the dynamical geometries studied in this work. It would be interesting to actually identify a theory of modified gravity which naturally gives rise to such configurations. One of the best explored phase spaces, comprising black hole type solutions in quadratic gravity, does not support such features [47–52].

APPENDIX A: CURVATURE INVARIANTS

In order to determine the physics consequences of perturbations on the geometry one should study the dynamics of physical observables. Quantities that naturally lend themselves to such a study are scalar quantities constructed from contractions of curvature tensors as, e.g., the Kretschmann scalar $K \equiv R_{\mu\nu\rho\sigma}R^{\mu\nu\rho\sigma}$ and the square of the Weyl tensor $C^2 \equiv C_{\mu\nu\rho\sigma}C^{\mu\nu\rho\sigma}$. In four spacetime dimensions these quantities are related by the identity

$$C^2 = K - 2R_{\mu\nu}R^{\mu\nu} + 1/3R^2. \tag{A1}$$

For vacuum solutions of general relativity, satisfying $R_{\mu\nu} = 0$, C^2 and K agree. Since the Reissner-Nordström solution and regular black hole solutions are not Ricci flat, these quantities can be different and in principle also exhibit different asymptotic scaling behaviors.

The metrics considered in this work take the form

$$ds^2 = -f(r,v)dv^2 + 2drdv + r^2d\Omega^2, \tag{A2}$$

where it is convenient to express the lapse function $f(r,v)$ in terms of the Misner-Sharp mass $M(r,v)$ through

$$f(r,v) = 1 - \frac{2M(r,v)}{r}. \tag{A3}$$

The curvature scalars obtained from (A2) then take the form

$$K = \frac{48M^2}{r^6} - \frac{64MM'}{r^5} + \frac{32(M')^2}{r^4}$$
$$+ \frac{16MM''}{r^4} - \frac{16M'M''}{r^3} + \frac{4(M'')^2}{r^2}, \tag{A4}$$

and

TABLE II. Specific form of the curvature scalars (A4) and (A5) evaluated for the Reissner-Nordström black hole (top line) and the three regular black hole geometries. The explicit form of the line element is given in the equations indicated in the second column. The coefficients k_i parametrizing the curvature for the RG-improved black hole are given in Eq. (A6).

Geometry	$f(r)$	K	C^2
Reissner-Nordström	Eq. (39)	$\dfrac{8(6m^2r^2-12mQ^2r+7Q^4)}{r^8}$	$\dfrac{48(Q^2-mr)^2}{r^8}$
Hayward	Eq. (11)	$\dfrac{48m^2(32l^8m^4-16l^6m^3r^3+72l^4m^2r^6-8l^2mr^9+r^{12})}{(2l^2m+r^3)^6}$	$\dfrac{48m^2r^6(r^3-4l^2m)^2}{(2l^2m+r^3)^6}$
RG-improved	Eq. (49)	$\dfrac{16m^2(3r^{12}+k_1\omega+k_2\omega^2+k_3\omega^3+k_4\omega^4)}{(9m\omega+r^3+2r\omega)^6}$	$\dfrac{16m^2r^2(54mr^2\omega+18m\omega^2-3r^5+2r^3\omega)^2}{3(9m\omega+r^3+2r\omega)^6}$
Bardeen	Eq. (50)	$\dfrac{12m^2(8a^8-4a^6r^2+47a^4r^4-12a^2r^6+4r^8)}{(a^2+r^2)^7}$	$\dfrac{12m^2r^4(3a^2-2r^2)^2}{(a^2+r^2)^7}$

$$C^2 = \frac{4(r^2M''-4rM'+6M)^2}{3r^6}. \qquad (A5)$$

Here the prime indicates derivatives with respect to r.

It is instructive to evaluate these curvature scalars for the (regular) black hole geometries discussed in the main part of this work. The results are compiled in Table II. The coefficients k_i appearing in the Kretschmann scalar for the RG-improved black hole are

$$k_1 = -4r^9(27m+r),$$
$$k_2 = 2r^6(2187m^2+432mr+26r^2),$$
$$k_3 = 2r^3(-2187m^3+972m^2r+252mr^2+16r^3),$$
$$k_4 = 2(19683m^4+11664m^3r$$
$$+ 3078m^2r^2+360mr^3+16r^4). \qquad (A6)$$

We observe that for the Reissner-Nordström geometry the curvature scalars diverge at $r=0$ owed to the vanishing of the denominator at this point. This signals the presence of a curvature singularity in the geometry. Regular black holes change the structure of this denominator in such a way that K and C^2 are bounded everywhere as long as $m>0$ and the model parameters are chosen properly. If $m<0$ the

denominators appearing in the Hayward and RG-improved cases may vanish though. It is this mechanism which underlies the power-law divergences of $K|_\Sigma^\infty$ and $C^2|_\Sigma^\infty$ reported in Table I.

The r-dependence of K and C^2 obtained for the Hayward geometry (11) is shown in Fig. 9. This illustrates the generic feature that K and C^2 do not agree for a regular black hole geometry due to extra contributions in Einstein's equations. While K increases monotonically, reaching a finite value at $r=0$, the C^2 invariant exhibits zeros at $r=0$ as well as one specific point located between the event and Cauchy horizons.

APPENDIX B: FROBENIUS ANALYSIS OF THE LATE-TIME ATTRACTOR

This appendix collects the technical details and subleading terms required in the consistent Frobenius analysis of the late-time attractor. The results for the Hayward black hole are discussed in detail in the text. The analogous formulas for the Reissner-Nordström geometry (RN), RG-improved black holes (RG), and the Bardeen black hole (B) are obtained along the same lines and summarized in Table III.
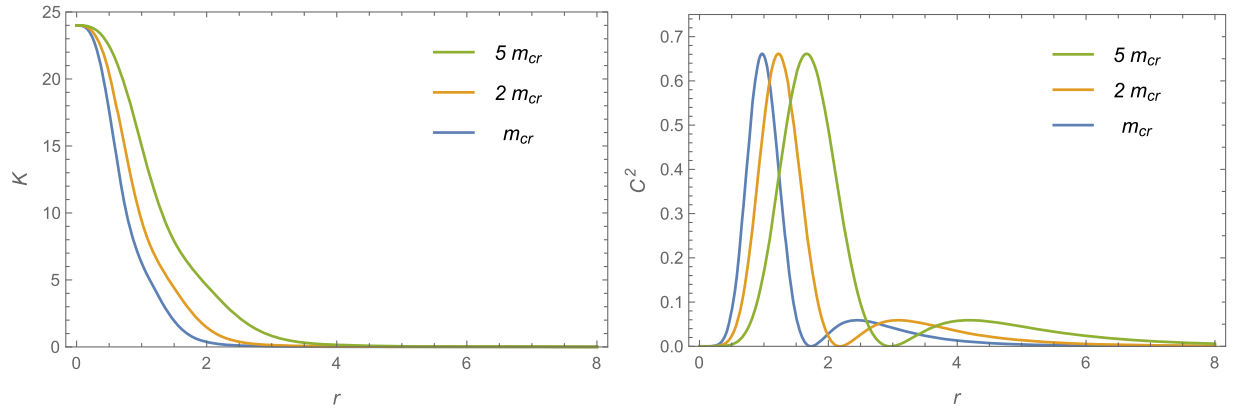

FIG. 9. Curvature scalars (A4) (top) and (A5) (bottom) evaluated for the Hayward geometry (11) with $l=1$.

TABLE III. Late-time expansion of the functions controlling the dynamics of the Ori model in the inner sector of the shell. The expansion order of each function is sufficient to arrive at the leading terms in the scaling behavior of the Misner-Sharp mass $M_+(v)|_\Sigma$ and the curvature scalars K and C^2 evaluated at the position of the shell.

$m_-(v)$	RN	$m_{cr} + \frac{30\pi m_{cr}^4}{v} + \frac{720\pi^{3/2}\sqrt{15}m_{cr}^{11/2}}{v^{3/2}} + (\tilde{m} + \text{nonanalytic})\frac{m_{cr}^7}{v^2}$
	RG ($\omega = 1$)	$m_{cr} + 1.35 \times 10^3 v^{-1} + 1.60 \times 10^8 v^{-3/2} + (\tilde{m} + \text{nonanalytic})v^{-2}$
	B ($a = 1$)	$m_{cr} + 2.86 \times 10^3 v^{-1} + 9.51 \times 10^5 v^{-3/2} + (\tilde{m} + \text{nonanalytic})v^{-2}$
$R(v)$	RN	$r_{cr} - \frac{2\sqrt{15\pi}r_{cr}^{5/2}}{\sqrt{v}} - \frac{(660\pi r_{cr}^2 + 1)r_{cr}^2}{2v} - \frac{1}{4096}(81\tilde{m}r_{cr}^4 - 315532800\pi^2 r_{cr}^4 - 30720\pi r_{cr}^2 + 512)(\frac{r_{cr}^3}{15\pi v^3})^{1/2}$
	RG ($\omega = 1$)	$r_{cr} - 7.35 \times 10^2 v^{-1/2} - 2.95 \times 10^5 v^{-1} + (2.83 \times 10^8 - 2.72 \times 10^{-3}\tilde{m})v^{-3/2}$
	B ($a = 1$)	$r_{cr} - 81.3 v^{-1/2} - 1.06 \times 10^4 v^{-1} + (2.02 \times 10^6 - 1.42 \times 10^{-2}\tilde{m})v^{-3/2}$
$F(v)$	RN	$-\sqrt{\frac{15\pi m_{cr}^3}{v}}$
	RG ($\omega = 1$)	$-84.5 v^{-1/2}$
	B ($a = 1$)	$-19.2 v^{-1/2}$
$m_+(v)$	RN	$m_{cr} + \frac{30\pi m_{cr}^4}{v} + \frac{720\sqrt{15}\pi^{3/2}m_{cr}^{11/2}}{v^{3/2}}$
	RG ($\omega = 1$)	$-8.04 + 4.11 \times 10^3 v^{-1/2} + 9.18 \times 10^5 v^{-1}$
	B ($a = 1$)	$1.30 + 2.86 \times 10^3 v^{-1}$
$M_+(v)|_\Sigma$	RN	$\frac{m_{cr}}{2}$
	RG ($\omega = 1$)	$-1.18v$
	B ($a = 1$)	5.20
$K|_\Sigma$	RN	$\frac{8}{m_{cr}^4}$
	RG ($\omega = 1$)	$2.40 \times 10^{-4} v^6$
	B ($a = 1$)	1.44
$C^2|_\Sigma$	RN	$\frac{2880\pi}{m_{cr}v}$
	RG ($\omega = 1$)	$8.00 \times 10^{-5} v^6$
	B ($a = 1$)	3.70×10^{-2}

The line element specifying the Hayward geometry is given in Eq. (11). The Frobenius analysis for the mass function $m_-(v)$ in the outer sector of the shell, taking into account the mass loss from Hawking radiation gives

$$m_-(v) \simeq m_{cr} + \frac{480\pi m_{cr}^4}{v} + 5120 m_{cr}^4 \left(\frac{5\pi m_{cr}}{v}\right)^{3/2}$$

$$+ \frac{m_{cr}^7}{v^2}(\tilde{m} + \text{nonanalytic}). \tag{B1}$$

Here the constant $\tilde{m}$ is not determined by the expansion. The occurrence of such a free parameter is expected, since we are approximating the solution to a first-order differential equation which comes with one integration constant fixing the solution. It is then remarkable that the first three terms in the expansion (B1) are universal in the sense that they are independent of these initial conditions. We also observe that the Frobenius expansion at $\mathcal{O}(v^{-2})$ requires the contributions of nonanalytic terms in order to ensure the cancellation of contributions appearing at $\mathcal{O}(v^{-3})$ in the expansion. Tracking these terms is beyond the scope of this work. While they may lead to logarithmic corrections to the scaling laws, they will not modify the power-law behavior of the quantities analyzed in this section.

In the next step, we analyze the late-time behavior of $R(v)$. The numerical analysis indicates that the shell approaches r_{cr} from below, i.e., from radii $r < r_{cr}$. We then select the corresponding sign in the leading term of the large-v expansion. This sign propagates also into the subleading coefficients, so that this branch of solutions has the expansion

$$R(v) \simeq r_{cr} - 3r_{cr}\left(\frac{15\pi r_{cr}^3}{v}\right)^{1/2} - r_{cr}^2\frac{1 + 585\pi r_{cr}^2}{2v}$$

$$+ \frac{r_{cr}^{3/2}(27(11686400\pi^2 - 3\tilde{m})r_{cr}^4 + 30720\pi r_{cr}^2 - 512)}{4096\sqrt{15\pi}v^{3/2}}. \tag{B2}$$

In order to ensure that the hierarchy of equations is solved consistently without contributions of higher-order terms missing in the expansion, we included the next term in (B2) and verified that it does not enter into the equations determining the coefficients in the expansion.

The next task is to determine the scaling of m_+ from Eq. (24). Here, we use the asymptotic form

$$m_+(v) \simeq -2m_{cr} + \frac{m_1}{\sqrt{v}} + \frac{m_2}{v}. \tag{B3}$$

In order to determine the free coefficients m_1 and m_2, two auxiliary considerations are in order. First, we use (B1) and (B2) to determine the scaling of the auxiliary function $F(v)$

$$F(v) \simeq -4m_{cr} \left(\frac{5\pi m_{cr}}{v} \right)^{1/2}. \qquad (B4)$$

Note that in this case, it actually suffices to retain the leading term in the expansion. The second observation is that for the late-time attractor (31) we must have

$$R^3 + 2l^2 m_+(v) \simeq \frac{d_1}{v}, \qquad (B5)$$

in order to have a consistent power-law solution compatible with the parametrization (B3). This fixes $m_1 = 48\sqrt{5\pi m_{cr}^5}$. With this knowledge, we can return to the full equation (24) and solve the first nontrivial order to fix m_2. This results in the asymptotic expansion

$$m_+(v) \simeq -2m_{cr} + 48\sqrt{\frac{5\pi m_{cr}^5}{v}} + \frac{2240\pi m_{cr}^4 + 8m_{cr}^2}{v}. \qquad (B6)$$

As an important corollary, we note that this implies that

$$d_1 = \frac{128 m_{cr}^4}{27v}. \qquad (B7)$$

Comparing Eq. (B5) with the definition of the Misner-Sharp mass in the inner sector of the shell, Eq. (11), and the results for the curvature scalars given in Table II, we note that it is actually the coefficient d_1 which sets the asymptotic scaling behavior of these quantities. Remarkably, (B7) is universal in the sense that it does not depend on initial conditions or any free parameters related to the dynamics of the solution. This establishes that the late-time behavior of the perturbed geometry is actually universal.

The Frobenius analysis for the Reissner-Nordström geometry literally proceeds along the same lines. In principle, the method is also applicable to the other geometries discussed in the main sections. In these cases the analysis is complicated by a proliferation of square-roots originating from the analytic expressions for the positions of the horizons. Following the strategy of determining the Frobenius coefficients exactly for arbitrary model coefficients ω and a leads to a significant increase in numerical complexity when simplifying expressions. In order to bypass this obstacle we then fix $\omega = 1$ and $a = 1$ and convert the analytic expression to high-precision floating numbers (tracking 50 digits). Based on the insights from the Hayward case, this allows to track the cancellation of leading and also subleading terms in the late-time expansion. The intermediate results leading to the late-time attractor described in Table I are collected in Table III for completeness.

APPENDIX C: GEODESIC EQUATIONS

In order to determine the geodesic structure of spacetime, we consider the motion of radially infalling observers and compute the relation between the coordinate v and the observer's proper time τ. Starting from the line element (A2), the v-component of the geodesic equation is

$$\ddot{v} = -\frac{1}{2} \frac{\partial f}{\partial r} \dot{v}^2, \qquad (C1)$$

where the dot represents a derivative with respect to proper time. The normalization for the four-velocity of the radial observer furthermore supplies the relation

$$L = \frac{1}{2}(f\dot{v}^2 - 2\dot{r}\dot{v}) = \frac{\epsilon}{2}. \qquad (C2)$$

with $\epsilon = 0$, 1 for lightlike or timelike geodesics, respectively. For a static geometry where f is independent of v,

$$\frac{\partial L}{\partial \dot{v}} = \text{const}, \qquad (C3)$$

is conserved along geodesic motion.

To understand the implications of the curvature singularities induced by the late-time attractors identified in Table I, we solve these equations for timelike geodesics close to the Cauchy horizon. Considering (C1), for a static, noncritical black hole, we first note that near the inner horizon

$$-\frac{1}{2} \frac{\partial f}{\partial r} \simeq \kappa_- > 0. \qquad (C4)$$

Equation (C1) is then readily solved in this limit, yielding the relation

$$\tau = \frac{1}{\kappa_-} e^{-\kappa_- v} + \text{const}. \qquad (C5)$$

The important insight from this result is that a massive observer can reach the singularity at $v = \infty$ in finite proper time. Hence the strength of the singularity becomes an important question when asking whether a geodesic can be continued beyond this point [30].

In the presence of Hawking radiation this analysis is radically altered though. In this case the late-time structure of spacetime is given by an extremal black hole where $\kappa_- = 0$. Therefore, Eq. (C1) gives the linear relation

$$\tau = cv + \text{const}. \qquad (C6)$$

with c an integration constant. The crucial difference to (C5) is that the timelike geodesic requires an infinite amount of proper time to reach $v = \infty$.

[1] S. W. Hawking and R. Penrose, The singularities of gravitational collapse and cosmology, Proc. R. Soc. A **314**, 529 (1970).

[2] L. Modesto, J. W. Moffat, and P. Nicolini, Black holes in an ultraviolet complete quantum gravity, Phys. Lett. B **695**, 397 (2011).

[3] T. De Lorenzo, C. Pacilio, C. Rovelli, and S. Speziale, On the effective metric of a Planck star, Gen. Relativ. Gravit. **47**, 41 (2015).

[4] A. Perez, No firewalls in quantum gravity: The role of discreteness of quantum geometry in resolving the information loss paradox, Classical Quantum Gravity **32**, 084001 (2015).

[5] A. Ashtekar and M. Bojowald, Black hole evaporation: A paradigm, Classical Quantum Gravity **22**, 3349 (2005).

[6] L. Bosma, B. Knorr, and F. Saueressig, Resolving Space-time Singularities within Asymptotic Safety, Phys. Rev. Lett. **123**, 101301 (2019).

[7] I. Dymnikova, Vacuum nonsingular black hole, Gen. Relativ. Gravit. **24**, 235 (1992).

[8] I. Dymnikova and E. Galaktionov, Stability of a vacuum nonsingular black hole, Classical Quantum Gravity **22**, 2331 (2005).

[9] J. M. Bardeen, Non-singular general-relativistic gravitational collapse, Proc. Int. Conf. GR5, Tbilisi 174 (1968).

[10] A. Bonanno and M. Reuter, Renormalization group improved black hole space-times, Phys. Rev. D **62**, 043008 (2000).

[11] B. Koch and F. Saueressig, Black holes within asymptotic safety, Int. J. Mod. Phys. A **29**, 1430011 (2014).

[12] A. Platania, Dynamical renormalization of black-hole spacetimes, Eur. Phys. J. C **79**, 470 (2019).

[13] F. Scardigli and G. Lambiase, Planck stars from asymptotic safe gravity, arXiv:2205.07088.

[14] C. Rovelli and F. Vidotto, Planck stars, Int. J. Mod. Phys. D **23**, 1442026 (2014).

[15] A. Barrau and C. Rovelli, Planck star phenomenology, Phys. Lett. B **739**, 405 (2014).

[16] F. Saueressig, N. Alkofer, G. D'Odorico, and F. Vidotto, Black holes in asymptotically safe gravity, Proc. Sci. FFP14 (**2016**) 174.

[17] S. A. Hayward, Formation and Evaporation of Regular Black Holes, Phys. Rev. Lett. **96**, 031103 (2006).

[18] T. Biswas, A. Conroy, A. S. Koshelev, and A. Mazumdar, Generalized ghost-free quadratic curvature gravity, Classical Quantum Gravity **31**, 015022 (2014).

[19] V. P. Frolov, Notes on nonsingular models of black holes, Phys. Rev. D **94**, 104056 (2016).

[20] J. Boos, Non-singular Gauss black hole from non-locality: A simple model with a de Sitter core, mass gap, and no inner horizon, arXiv:2104.00555.

[21] A. Biasi, O. Evnin, and S. Sypsas, De Sitter bubbles from anti-de Sitter fluctuations, arXiv:2209.06835.

[22] F. Saueressig and A. Khosravi, Black hole remnants from dynamical dimensional reduction?, Phys. Rev. D **105**, 066015 (2022).

[23] D. N. Page, Particle emission rates from a black hole. II. Massless particles from a rotating hole, Phys. Rev. D **14**, 3260 (1976).

[24] D. Harlow, Jerusalem lectures on black holes and quantum information, Rev. Mod. Phys. **88**, 015002 (2016).

[25] J. Polchinski, The black hole information problem, in Theoretical Advanced Study Institute in Elementary Particle Physics: New Frontiers in Fields and Strings (World Scientific Publishing, London, 2017), pp. 353–397.

[26] V. P. Frolov, Remarks on non-singular black holes, EPJ Web Conf. **168**, 01001 (2018).

[27] R. Carballo-Rubio, F. Di Filippo, S. Liberati, C. Pacilio, and M. Visser, On the viability of regular black holes, J. High Energy Phys. 07 (2018) 023.

[28] E. Poisson and W. Israel, Internal structure of black holes, Phys. Rev. D **41**, 1796 (1990).

[29] A. Ori, Inner Structure of a Charged Black Hole: An Exact Mass-Inflation Solution, Phys. Rev. Lett. **67**, 789 (1991).

[30] A. Bonanno, A.-P. Khosravi, and F. Saueressig, Regular black holes with stable cores, Phys. Rev. D **103**, 124027 (2021).

[31] A. J. S. Hamilton and P. P. Avelino, The Physics of the relativistic counter-streaming instability that drives mass inflation inside black holes, Phys. Rep. **495**, 1 (2010).

[32] C. Barrabes and W. Israel, Thin shells in general relativity and cosmology: The lightlike limit, Phys. Rev. D **43**, 1129 (1991).

[33] R. H. Price, Nonspherical perturbations of relativistic gravitational collapse. I. Scalar and gravitational perturbations, Phys. Rev. D **5**, 2419 (1972).

[34] R. H. Price, Nonspherical perturbations of relativistic gravitational collapse. II. Integer-spin, zero-rest-mass fields, Phys. Rev. D **5**, 2439 (1972).

[35] R. Penrose, in Battelle Rencontres, edited by C. M. De Witt and J. A. Wheeler (Benjamin, New York, 1968).

[36] A. Bonanno, S. Droz, W. Israel, and S. M. Morsink, Structure of the spherical black hole interior, Proc. R. Soc. A **450**, 553 (1995).

[37] S. W. Hawking, Particle creation by black holes, Commun. Math. Phys. **43**, 199 (1975); Erratum, Commun. Math. Phys. **46**, 206 (1976).

[38] R. Carballo-Rubio, F. Di Filippo, S. Liberati, C. Pacilio, and M. Visser, Inner horizon instability and the unstable cores of regular black holes, J. High Energy Phys. 05 (2021) 132.

[39] F. Di Filippo, R. Carballo-Rubio, S. Liberati, C. Pacilio, and M. Visser, On the inner horizon instability of non-singular black holes, Universe **8**, 204 (2022).

[40] L. M. Burko, Strength of the null singularity inside black holes, Phys. Rev. D **60**, 104033 (1999).

[41] F. J. Tipler, Singularities in conformally flat spacetimes, Phys. Lett. **64A**, 8 (1977).

[42] V. Cardoso, J. a. L. Costa, K. Destounis, P. Hintz, and A. Jansen, Quasinormal Modes and Strong Cosmic Censorship, Phys. Rev. Lett. **120**, 031103 (2018).

[43] S. Hollands, R. M. Wald, and J. Zahn, Quantum instability of the Cauchy horizon in Reissner–Nordström–deSitter spacetime, Classical Quantum Gravity **37**, 115009 (2020).

[44] E. Ayon-Beato and A. Garcia, The Bardeen model as a non-linear magnetic monopole, Phys. Lett. B **493**, 149 (2000).

[45] R. Carballo-Rubio, F. Di Filippo, S. Liberati, C. Pacilio, and M. Visser, Regular black holes without mass inflation instability, J. High Energy Phys. 09 (2022) 118.

[46] E. Franzin, S. Liberati, J. Mazza, and V. Vellucci, Stable rotating regular black holes, Phys. Rev. D **106**, 104060 (2022).

[47] A. Bonanno and S. Silveravalle, The gravitational field of a star in quadratic gravity, J. Cosmol. Astropart. Phys. 08 (2021) 050.

[48] A. Bonanno and S. Silveravalle, Characterizing black hole metrics in quadratic gravity, Phys. Rev. D **99**, 101501 (2019).

[49] J. Podolsky, R. Svarc, V. Pravda, and A. Pravdova, Black holes and other exact spherical solutions in quadratic gravity, Phys. Rev. D **101**, 024027 (2020).

[50] J. Podolsky, R. Svarc, V. Pravda, and A. Pravdova, Black Holes and other Exact Spherical Solutions in Quadratic Gravity, Phys. Rev. Lett. **121**, 231104 (2018).

[51] F. Saueressig, M. Galis, J. Daas, and A. Khosravi, Asymptotically flat black hole solutions in quadratic gravity, Int. J. Mod. Phys. D **30**, 2142015 (2021).

[52] J. Daas, K. Kuijpers, F. Saueressig, M. F. Wondrak, and H. Falcke, Probing quadratic gravity with the Event Horizon Telescope, arXiv:2204.08480.